applied optics

Low-frequency noise effect on terahertz tomography using thermal detectors

J. P. Guillet,[1,*] B. Recur,[2] H. Balacey,[3] J. Bou Sleiman,[1] F. Darracq,[1] D. Lewis,[1] and P. Mounaix[1]

[1]IMS, Bordeaux University, CNRS UMR 5218, 351 cours de la Liberation, 33405 Talence, France
[2]Australian National University, Department of Applied Mathematics RSPE, Canberra, Australia
[3]Noctylio S.A.S., 59 cours de l'Intendance, 33000 Bordeaux, France
*Corresponding author: jean-paul.guillet@u-bordeaux.fr

Received 30 April 2015; revised 7 July 2015; accepted 7 July 2015; posted 8 July 2015 (Doc. ID 239974); published 27 July 2015

In this paper, the impact of low-frequency noise on terahertz-computed tomography (THz-CT) is analyzed for several measurement configurations and pyroelectric detectors. We acquire real noise data from a continuous millimeter-wave tomographic scanner in order to figure out its impact on reconstructed images. Second, noise characteristics are quantified according to two distinct acquisition methods by (i) extrapolating from experimental acquisitions a sinogram for different noise backgrounds and (ii) reconstructing the corresponding spatial distributions in a slice using a CT reconstruction algorithm. Then we describe the low-frequency noise fingerprint and its influence on reconstructed images. Thanks to the observations, we demonstrate that some experimental choices can dramatically affect the 3D rendering of reconstructions. Thus, we propose some experimental methodologies optimizing the resulting quality and accuracy of the 3D reconstructions, with respect to the low-frequency noise characteristics observed during acquisitions.

OCIS codes: (110.6795) Terahertz imaging; (110.6955) Tomographic imaging; (100.6890) Three-dimensional image processing; (170.3010) Image reconstruction techniques; (120.5800) Scanners; (000.2700) General science.

http://dx.doi.org/10.1364/AO.54.006758

1. INTRODUCTION

The low photon energy of terahertz (THz) waves has made THz imaging an emerging technique used in the fields of security, and contact-free and nondestructive testing. Due to sufficient transparency and good penetration lengths in various materials, especially below 1 THz, this technique leads to innovations in technologies taking advantages from two outstanding ideas and the concepts of each field. Then imaging and sensing systems based on THz radiation have been proposed several decades ago, in analogy to similar systems and corresponding applications developed from both optical and microwave radiations.

The THz-time domain system (THz-TDS) is one the most popular techniques [1–4] allowing, for instance, the determination of the complex permittivity of a sample over a frequency range (typically, 0.1–4 THz) for each pixel under investigation. The data acquisition, which can be performed in transmission or in reflection, provides information about the static properties of the sample over its frequency spectrum at each pixel. Despite clear benefits, performing image analysis with THz-TDS deals with some restrictions. For instance, the power generated in the THz beam is quite low, so that it has to be associated with very high-dynamic-range instruments. Moreover, most of the time-domain imaging systems are based on a raster scanning of the sample since no array of coherent detectors is available. This considerably slows down both the image acquisition rate and the reconstruction time of a series of single-point measurements. Another limitation is due to the sampling technique used to reconstruct the time response of the beam. Typically, the spectral resolution is inversely proportional to the temporal window used during the acquisition. Thus, we have to deal with a trade-off between acquisition time and spectral resolution. Recently, very promising solutions were proposed about the design of compact and inexpensive THz imaging systems relying on femtosecond fiber laser technology without a mechanical stage (see, for example, ECOPS [5], ASOPS [6], and OSCAT [7] techniques).

Another way to create 3D images from THz or sub-THz imaging systems is to compensate for the lack of THz-TDS phase information by acquiring a set of 2D projections distributed around the sample. Then a tomographic reconstruction algorithm provides a 3D volume imaging of the acquired object by combining all projection data. THz-computed tomography (THz-CT), introduced by Fergusson *et al.* in 2002, has the advantage to provide a 3D representation of the sample. However, all existing techniques developed over decades for x-ray tomography have to be revisited since THz beam propagation is far from that of the x-ray one. Nevertheless, it has been

demonstrated that this technique is able to perform 3D reconstructions at different frequencies in order to extract information about the target. Upcoming research in this domain aims at focusing on the improvement of the THz beam modeling used in THz-CT algorithms to allow reconstructions of complex targets in the presence of noise.

Especially in our current works, we focus our attention on the consequences of low-frequency noise on THz-CT acquisitions and corresponding reconstructed images [8–10]. The absorption during THz propagation through a sample can be high enough to make the noise level greater than the transmitted signal. Thus, this noise becomes the main recorded and reconstructed information. We first simulate the noise influence in order to give an insight on the noise artifact. To this aim, we acquire real noise data using different THz detectors plugged into a continuous-wave tomographic scanner. Particularly, we experiment pyroelectric sensors and Schottky diodes, which have different low-frequency noise sources [11,12]. Then the noise features are examined following two different raster scanning trajectories. For each scanning procedure, the noise background is processed to provide a sinogram (a set of 1D projections) and the corresponding spatial distribution in a slice. Then we discuss the low-frequency noise fingerprint on the CT reconstructions. We demonstrate that some experimental choices can dramatically affect the quality and accuracy of 3D reconstructions. For example, in the case of absorbing or thick samples, the results obtained could simply be the reconstruction of noise.

2. THZ-COMPUTED TOMOGRAPHY

A. Experimental Setup

The 3D millimeter-wave tomographic scanner used in this work is shown in Fig. 1. The source is a Gunn diode coupled with a horn antenna with a frequency of 84 GHz, which can be coupled with a frequency tripler. The system generates a beam with a central frequency of 252 GHz and power of 14 mW focused by an assembly of four polytetrafluoroethylene (PTFE) lenses ($f = 50$ mm focal length and $D = 50$ mm diameter). The sample is positioned on a three-axis motorized stage comprising X, Y, and θ movements. The detection is performed by a pyroelectric sensor and a lock-in amplifier associated with a mechanical chopper modulating the signal with a frequency of 25 Hz. As an alternative, the pyroelectric sensor could be replaced with a Schottky diode.

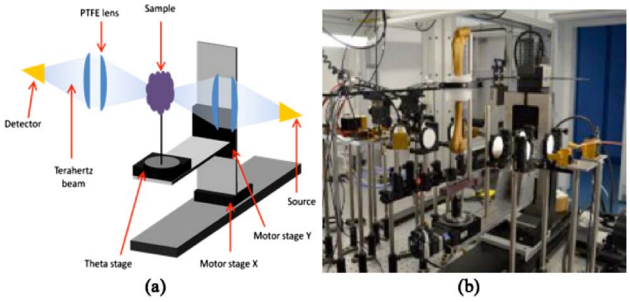

Fig. 1. (a) Experimental setup scheme of the 3D millimeter-wave tomographic scanner. (b) Photograph of the setup with both 84 and 252 GHz sources.

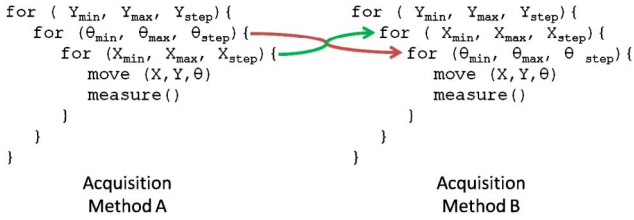

Fig. 2. Different loops for acquisition method A and B algorithms.

B. Acquisition Methods

Acquisition consists of a raster scanning, which creates a 3D array of data. It uses three movements, corresponding to each axis, implemented by three "for" loops along X, Y, and θ axes. This process can be configured following six permutations corresponding to the acquisition order. Due to hardware limitations in terms of the acquisition speeds of the different stages, we consider that the main acquisition loop is Y axis. Consequently, we propose to consider two different acquisitions of the (X, θ) sinogram, denoted A and B, whose algorithms are summarized in Fig. 2. Both the acquisition methods acquire the same matrix of points but with two different sequences. Method A sequentially acquires all points in a row, then iterates to the subsequent projection θ (acquisition row by row). Conversely, method B acquires all points at a given x position for all projections (by moving the rotation stage), then iterates the process for all x positions (acquisition column by column). Thus, the noise distribution is different onto the scanned area since the variations are time-dependent and the noise is correlated to a random characteristic of all electronic sensors. The sinogram data array (X, θ) is the input of a CT reconstruction algorithm that allows reconstructing a 2D image (X, Z), corresponding to a thick surface (denoted slice) of the noise distribution.

3. LOW-FREQUENCY NOISE IMPACT ON TOMOGRAPHY

A. THz Detector Noise

The noise generated by electronic devices varies greatly as different effects can produce it. Thermal noise is compulsory, whereas other types depend mostly on device type physical defects, including $1/f$ noise. THz thermal detectors like pyroelectric and bolometer detectors present several noise sources [12–16]. The pyroelectric detector used in this work suffers from (i) Johnson noise, induced by pyroelectric conductance, (ii) voltage noise, generated by the amplifying circuit, (iii) temperature fluctuation noise, and (iv) current noise. Johnson noise is white with resistive materials and presents frequency dependence with the pyroelectric detector due to its capacitive property. The pyroelectric mean square Johnson noise is given by

$$V_N^2 = \frac{kT}{\omega C \tan \delta}, \tag{1}$$

where k is the Boltzmann constant, T is the temperature, ω is the angular frequency, C is the capacity, and $\tan \delta$ is the dielectric loss. From Eq. (1) we can deduce that noise increases strongly when $\omega \to 0$. At low frequencies, i.e., when

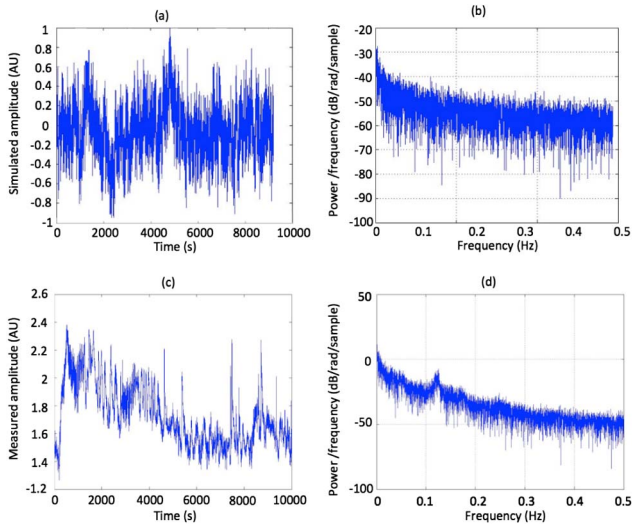

Fig. 3. (a) Simulation of low-frequency noise in the pyroelectric detector. (b) Power spectral density of the simulation. (c) Data acquired over 10,000 s. (d) Power spectral density of the acquired data.

$f < 1$ Hz, Johnson noise is overriding [17]. This low-frequency noise, also called pink noise, is predominant and we could simulate it using Matlab code. For instance, Figs. 3(a) and 3(b) show typical results concerning, respectively, the temporal and frequency spectra of such a simulated noise.

B. Experimental Noise Acquisition

We now perform noise data acquisition from the setup. In order to reduce other possible noise sources, due to motor stage precision or vibrations, we actually acquire data without stage motion so that the acquisition consists of a direct transmission from the emitter to the detector. To mimic the attenuation of a slightly transparent object, we add an absorber layer inducing a signal attenuation and strongly deteriorating the signal-to-noise ratio (SNR). We collect 10,000 points with a 0.5 Hz sampling frequency rate. The acquisition time is about 3 h and 30 min. The locking amplifier modulation frequency is 25 Hz, the time constant is 100 ms, and the slope is 12 dB/oct. These parameters follow the lock-in amplifier specifications, thus avoiding the addition of low-frequency noise due to the locking amplifier itself. We repeat these acquisitions several times and average the values. In Figs. 3(c) and 3(d), we plot the power spectral density and frequency spectrum of the acquired noise data. Their relative magnitude and variation with frequency are in good agreement with the simulated noise spectra. We observe that Johnson noise is predominant above 20 Hz and the main noise source is linked to the resistor presence below. As soon as we can numerically reproduce the variation of the noise, we can undertake some calculations with the acquired sinograms and analyze their impacts on the reconstructed images.

C. Noise Fingerprint in Sinograms

We now allocate the same acquired noise data shown in Fig. 3(c) to the matrix of points according to both the acquisition sequences introduced in Section 2.B. Due to low-frequency noise, fluctuations over long periods create lines in the sinograms following the same direction as the raster

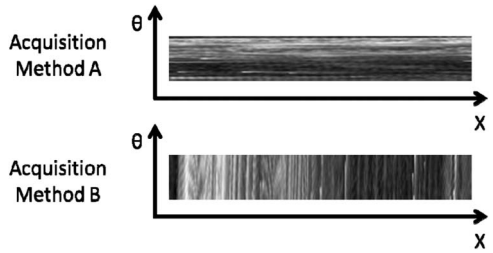

Fig. 4. Sinograms of the noise acquisition allocating data with respect to acquisition method A or B.

scanning subloop, as shown in Fig. 4. This effect is visible and is common for all raster scanning systems with pink noise, and can be observed in various fields such as astronomy [18], THz near-field imaging [19], or optical coherence tomography [20]. So the so-called sinogram for a slice contains orthogonal or parallel lines with respect to X axis. We can expect that such feature differences between both acquisitions will induce very different features into the reconstructed tomographic data.

D. Combination of Acquired Noise and Shepp–Logan Phantom Reconstruction

The aim of this section is to evaluate the effect of low-frequency noise on the tomographic images by acquiring the sinogram data of a sample and roughly adding to it the pink noise sinogram of the same size. We illustrate our development by using the very-well-known Shepp–Logan phantom, sized 256 × 256 pixels [cf. Fig. 5(a)]. A simulated acquisition based on the Radon transform is performed on this phantom in order to obtain 36 tomographic projections uniformly distributed between 0° and 180° (angular step of 5°). Then we reconstruct the image from such a sinogram using the reconstruction method called backprojection of filtered projections (BFP). We can notice in the resulting image [cf. Fig. 5(b)] that many artifacts related to BFP surround the reconstructed object. BFP is particularly sensitive to the noise and it is unable to reconstruct accurately the slice from a few number of projections. We can notice that this reconstruction does not recover exactly the initial phantom. The contrast is lower and the homogeneity of regions is lost (especially for the largest dark gray region). Moreover, a grainy texture appears everywhere, leading to the quasi-disappearance of small details. All these reconstruction artifacts are mainly

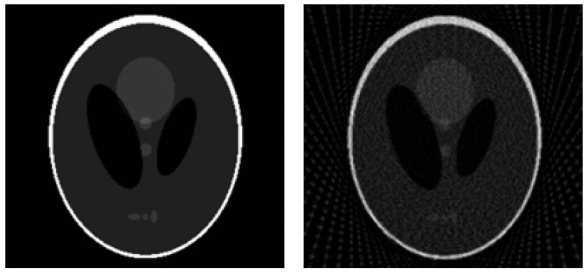

Fig. 5. (a) Original Shepp–Logan phantom sized 256 × 256 pixels. (b) Reconstruction using 36 projections with the BFP algorithm. It highlights the reconstruction artifacts.

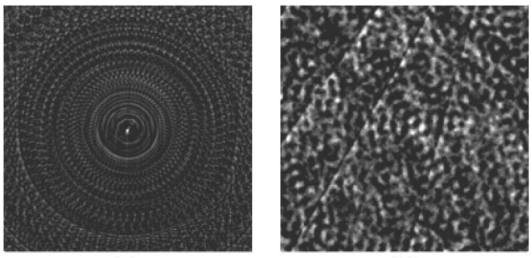

Fig. 6. Difference between reconstructed noise characteristics: (a) from noise sinogram obtained by method A and (b) from noise sinogram obtained by method B.

inherent to the BFP algorithm when using a number of projections quite smaller than the image size ($36 \ll 256$). However, we usually acquire 36 projections with a raster scanning system to have a good trade-off between reconstruction accuracy and time acquisition.

Figure 6 shows the images of typical noise fingerprints obtained by CT reconstruction from the noise sinograms given in Fig. 4. They are quite obviously different, as we expected in Section 3.C. Indeed, trajectory A leads to a circular symmetry and a hot spot in the center of the image, whereas the second fingerprint, obtained from sinogram B, is spotty, with grains and several marked lines.

Each noise sinogram (Fig. 4) is now considered a noise reference to be added to a sinogram of a sample. We add each noise sinogram to the acquired sinogram of the Shepp–Logan phantom with different coefficients corresponding to significant SNRs, 0, 3, and 10 dB, with respect to the signal level. These signal levels are commonly encountered in real experiments when we acquire thick or absorptive samples. The results of the reconstructions, which are performed following both schemes A and B, are presented in Fig. 7. We can identify noise the fingerprints described in Fig. 6, which are overprinting the original reconstructed image [Fig. 5(b)]. With method A, the central point saturates the image and circles are quite visible. When using method B, smooth points are superimposed to the original image. In that case, method A gives a better rendering of the edges, whereas method B has no ring artifact.

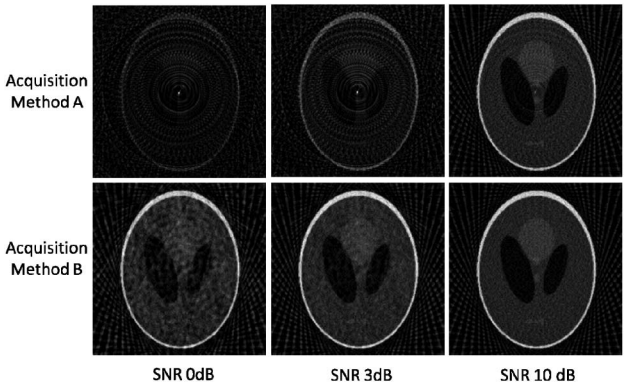

Fig. 7. BFP reconstructions of the Shepp–Logan phantom from noisy sinograms with different SNRs and using acquisition schemes A and B.

From the observation, we can conclude that the noise harms the interpretation of the reconstruction differently, depending on the characteristics about the sample and the sweeping of the acquisition. In all the cases, BFP artifacts are majority present outside the area of interest, although some lines still appear in the area of interest.

4. STUDY CASES

We now study the reconstruction of two different samples, compare the noise influence on the reconstructions, and propose experimental solutions to reduce the noise effect.

A. Cylindrical Symmetry Sample

We propose to study the case of an object with cylindrical symmetry, comparable to a pottery or a conduit with several layers, for instance. The original perfect object is represented in Fig. 8(a). The reconstructed object, obtained by BFP from 36 projections (without noise addition), is shown in Fig. 8(b). We can notice the presence of particularly intense spots around the external area of the object. A small influence in the center is also reported. This aspect could be reduced by increasing the number of projections. Then we follow the same procedure to evaluate the noise features onto the reconstructed slice. To emphasize the noise effect, we add to the sinogram of the object the noise acquired by our THz setup with a SNR of 0 dB, in a similar manner to that in Section 3.D. When we apply the acquisition scheme A, several artifact circles dramatically affect the original image, as shown in Fig. 8(c). Thus, the shapes corresponding to the original object become very difficult to distinguish from circles due to noise. Furthermore, close circles cannot be resolved and no symmetry can be assumed without the original image eye guideline. Similarly, we add the noise sinogram to the sinogram of the object using scheme B and reconstruct with BFP [cf. the result image in Fig. 8(d)].

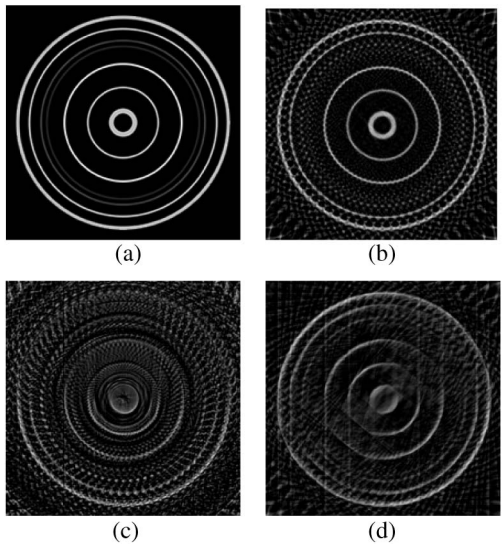

Fig. 8. (a) Slice view of the original cylindrical symmetry sample. (b) BFP reconstruction from noise-free sinogram. (c) BFP reconstruction from the sinogram after addition of method A noise. (d) BFP reconstruction from the sinogram after addition of method B noise.

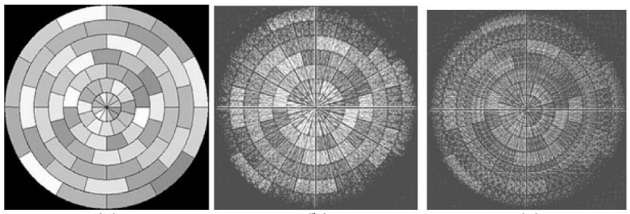

Fig. 9. (a) Slice view of the original cylindrical symmetry sample. BFP reconstruction after adding noise following (b) method A and (c) method B.

Although the noise level is equivalent, its distribution in the picture is significantly different and we can recognize the circles of the original image despite the same noise level. The circular aspect of the noise signature of method A is not recommended for objects having an internal structure with cylindrical symmetry.

B. More Complex Sample

While the first case study was proposed to assess the geometric fidelity rendering, the second one is designed to assess the contrast fidelity. This second object is a checker pattern target with different gray variations depending on the axial coordinate and angular position. It is a very complicated case.

We can see in Figs. 9(b) and 9(c) that we obtain better contrast with method A than with method B. We can explain this by the concentration of noise in several circles with method A, which avoids the degradation of gray levels. In case B, noise acts as spots distributed randomly, leading to detail losses inside the object and a lower resolution.

5. DISCUSSION AND OUTLOOK

Due to different spatial distributions of the low-frequency noise, we have demonstrated that the design of the acquisition can affect the aspect of the reconstructed images. Whatever the acquisition scheme, artifacts may occur, degrading the reconstruction quality. It should be noted that this is only important for opaque objects and only if the SNR is low (3 dB or less). Moreover, for THz sources and detectors having poor SNRs, this work suggests that we have to take care of the acquisition procedure depending on the symmetry and morphology of the internal features. Method A is the finest for both edge and dynamic preservations, but it could add extra circles to the image when the SNR is low (in opaque areas of the sample). Method B should be chosen if the object analyzed is cylindrical or contains cylindrical substructures because the low-frequency noise circles would be confusing if we use scheme A. These results could be useful for the physical interpretation of spotty surfaces observed after the tomography reconstruction of unknown samples since they could no longer characterize the object texture but the noise fingerprint.

REFERENCES

1. D. M. Mittleman, *Sensing with Terahertz Radiation* (Springer, 2003).
2. X. C. Zhang and J. Z. Xu, *Introduction to THz Wave Photonics* (Springer, 2009).
3. Y. S. Lee, *Principles of Terahertz Science and Technology* (Springer, 2009), p. 349.
4. S. L. Dexheimer, *Terahertz Spectroscopy: Principles and Applications* (CRC Press, 2008).
5. K. H. Jin, Y.-G. Kim, S. H. Cho, J. C. Ye, and D.-S. Yee, "High-speed terahertz reflection three-dimensional imaging for nondestructive evaluation," Opt. Express **20**, 25432–25440 (2012).
6. A. Bartels, R. Cerna, C. Kistner, A. Thoma, F. Hudert, C. Janke, and T. Dekorsy, "Ultrafast time-domain spectroscopy based on high-speed asynchronous optical sampling," Rev. Sci. Instrum. **78**, 035107 (2007).
7. R. Wilk, T. Hochrein, M. Koch, M. Mei, and R. Holzwarth, "OSCAT: novel technique for time-resolved experiments without moveable optical delay lines," J. Infrared Millimeter Terahertz Waves **32**, 596–602 (2011).
8. B. Recur, A. Younus, S. Salort, P. Mounaix, B. Chassagne, P. Desbarats, J. P. Caumes, and E. Abraham, "Investigation on reconstruction methods applied to 3D terahertz computed tomography," Opt. Express **19**, 5105–5117 (2011).
9. J. P. Guillet, B. Recur, L. Frederique, B. Bousquet, L. Canioni, I. Manek-Hönninger, P. Desbarats, and P. Mounaix, "Review of terahertz tomography techniques," J. Infrared Millimeter Terahertz Waves **35**, 382–411 (2014).
10. B. Recur, H. Balacey, J. Bou Sleiman, J. Perraud, J.-P. Guillet, A. Kingston, and P. Mounaix, "Ordered subsets convex algorithm for 3D terahertz transmission tomography," Opt. Express **22**, 23299–23309 (2014).
11. S. Liu and D. Long, "Pyroelectric detectors and materials," Proc. IEEE **66**, 14–26 (1978).
12. G. A. Burdick and R. T. Arnold, "Theoretical expression for the noise equivalent power of pyroelectric detectors," J. Appl. Phys. **37**, 3223–3226 (1966).
13. S. T. Liu and D. Long, "Pyroelectric detectors and materials," Proc. IEEE **66**, 14–26 (1978).
14. S. E. Stokowski, "Temperature noise and dielectric loss in pyroelectric detectors," Appl. Phys. Lett. **29**, 393–395 (1976).
15. P. W. Kruse, *Uncooled Thermal Imaging: Arrays, Systems, and Applications* (SPIE, 2001), Vol. **2003**.
16. J. C. Mather, "Bolometer noise: nonequilibrium theory," Appl. Opt. **21**, 1125–1129 (1982).
17. R. W. Whatmore, "Pyroelectric devices and materials," Rep. Prog. Phys. **49**, 1335–1386 (1986).
18. D. T. Emerson and R. Gräve, "The reduction of scanning noise in raster scanned data," Astron. Astrophys. **190**, 353–358 (1988).
19. J. P. Guillet, L. Chusseau, R. Adam, T. Grosjean, A. Penarier, F. Baida, and D. Charraut, "Continuous-wave scanning terahertz near-field microscope," Microwave Opt. Technol. Lett. **53**, 580–582 (2011).
20. H. Yu, J. Jang, J. Lim, J.-H. Park, W. Jang, J.-Y. Kim, and Y. Park, "Depth-enhanced 2-D optical coherence tomography using complex wavefront shaping," Opt. Express **22**, 7514–7523 (2014).